Excimer Laser-Annealing of Amorphous Silicon Layers

J. Förster[*,1] and H. Vogt[1]
[1]Institute of Electronic Components and Circuits, University Duisburg-Essen, Germany

*Corresponding author: Jan Förster, University Duisburg-Essen, Bismarckstr. 81, 47057 Duisburg, Germany, Email: jan.foerster@uni-due.de

Abstract: This paper describes a one-dimensional model of excimer laser-annealing of amorphous silicon layers which are irradiated with a pulsed KrF excimer laser. For realisation of the model in COMSOL Multiphysics, the application mode heat transfer in solids is used. The model predicts a melt threshold for the energy density of the laser of $E_{\mathrm{th}} = 88.5$ mJ/cm^2. It also predicts a linear increase of the melt duration with a slope of approximately $\partial t_{\mathrm{m}}/\partial E = 625$ ns cm^2 J^{-1} and a decrease of the onset time to melt from $t_{on} = 28$ ns down to some nanoseconds with enhanced energy density of the laser. Concerning the melt depth, the simulations return a linear slope of $\partial d_{\mathrm{m}}/\partial E = 43$ µm cm^2 J^{-1} with increasing energy density. All these results are in excellent agreement with the results of our experiments and therefore, the validity of our model is confirmed.

Keywords: Phase Transition, Melting, Excimer Laser-Annealing (ELA), Amorphous Silicon (a-Si), Thermal Load.

1. Introduction

Annealing of amorphous semiconductor materials like amorphous silicon (a-Si) which are deposited on substrates with a low thermal budget, for example glass, polymers, or completed CMOS structures, is a major challenge. These substrates do not allow furnace annealing, but require an annealing technique which affects only the uppermost layer. Therefore, annealing of such materials by laser irradiation is a well-established technique, called laser-annealing (LA) [1]. To minimize the thermal stress of the substrates, it is necessary to use a pulsed laser with both a short wavelength and a short pulse duration [2]. Excimer lasers fit these needs very well and, therefore, Excimer Laser-Annealing (ELA) is an adequate technique for annealing materials on temperature-limited substrates. Successfully demonstrated for the first time by Yaron et al. in 1980 [3], ELA has now become a standard technique in modern CMOS processes [4].

The laser energy is absorbed in the sample and transformed into heat during the laser-annealing process. If the heat exceeds the melting point of the processed amorphous material, the material will melt and it will generally form polycrystalline structures during re-solidification. In addition, potentially existing dopants will be electrically activated. However, this electrical activation can already occur at temperatures just under the melting point of the amorphous material [5]. This later version of electrical activation is preferred for the production of thin-film transistors and optical sensors.

We want to use ELA as a step in the production of a-Si based sensors on top of completed CMOS structures. As a thermal limitation, these CMOS structures must not be heated above $T_{\max} = 400$°C to avoid any damage to these structures. Thus, we have to know the thermal load of the substrates caused by ELA to determine optimised process parameters. Furthermore, the a-Si layer for some of the sensors must not melt, so we also need to know the maximum applicable laser energy for non-melt ELA.

Determination of the values for the thermal load and the maximum applicable laser energy by experiments is expensive and very time-consuming. A much faster and cost-effective way to identify these values is running simulations. Moreover, modelling of the ELA allows easy adaption of our different sensor types. Therefore, we set up a model for ELA of thin a-Si layers. To validate our model, we compare its results with the results of our ELA experiments regarding the values for the melt duration, onset time to melt, the melt threshold, and the melt depth.

In this paper, we discuss our model of ELA of a-Si layers. First, the design of our model, which is based on the samples we used in our previous ELA experiments, is described in section 2. Fundamental equations and relations as well as their realisation in COMSOL Multiphysics are explained in sections 3 and 4 respectively. The results of our model are presented and compared to the experimental data in section 5.

2. The model

In our ELA experiments we measured the electrical conductivity as a function of the energy density of the laser [6]. Amongst others, these measurements were used to extract the minimum value of the energy density, for which melting of the a-Si layer occurs. We performed the ELA experiments for different initial sample temperatures to study the influence of the initial sample temperature on this melt threshold. Afterwards, some of the samples were analysed for microcrystalline structures with SEM. In addition, we performed time-resolved reflectivity measurements (TRRM) in the way they have been described by Jellison et al. [7] to analyse the melt duration and the onset time to melt as a function of the energy density.

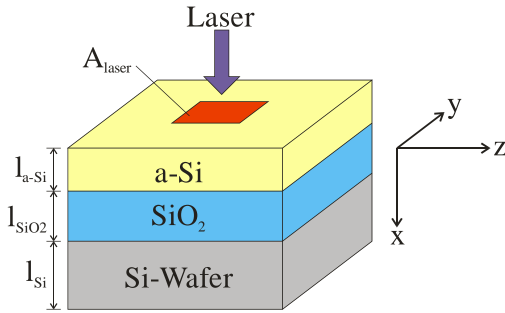

Figure 1. Schematic drawing of the samples used for the ELA experiments.

In these experiments we used a pulsed KrF excimer laser (wavelength $\lambda_{KrF} = 248$ nm, FWHM pulse duration $t_{pulse} = 25$ ns) to irradiate a square array (feed size $l_{laser} = 5$ mm) of our samples. As shown in Figure 1, the samples consisted of a 750 µm thick silicon wafer (l_{Si}), which had been coated with a 1000 nm thick layer of silicon dioxide SiO_2 (l_{SiO2}) to supress lattice distortion on the one hand and for electrical insulation on the other hand. On top of the SiO_2 we deposited a 250 nm thick a-Si layer ($l_{a\text{-}Si}$).
To get comparable results from the simulations, we use our experimental setup as basis for our model. Fortunately, the laser is homogeneously distributed at the surface of the irradiated sample due to the optical elements in its path. In addition, the lateral dimensions of the processed area of our samples are much bigger than their vertical dimension by several orders of magnitude. Thus, we can neglect lateral effects and reduce the problem to a one-dimensional model along the x-axis as it is shown in Figure 2 [8]. Each layer of the sample is represented by an interval (i1, i2, and i3) whose length equals the corresponding layer

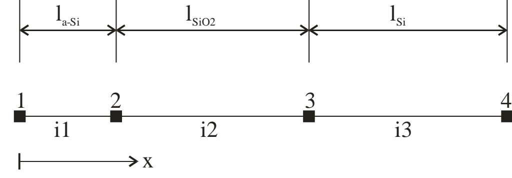

Figure 2. Implementation of the sample geometry into our one-dimensional model.

thickness. The surface of the sample (x = 0) and the bottom side of the sample are located in the points 1 and 4 respectively. The interfaces between the layers are given by the points 2 and 3.

3. Governing Equations

As shown by Baeri and Camisano [8], the heating of material by laser light can be expressed by

$$\frac{\partial T}{\partial t} = \frac{\alpha}{\rho \cdot C_p} I(x,t) + \frac{1}{\rho \cdot C_p} \frac{\partial}{\partial x}\left(\kappa \frac{\partial T}{\partial x}\right), \quad (1)$$

where *I(x,t)* is the power density of the laser light at depth *x* and time *t*, *T* is the temperature, and ρ, C_p, κ, and α are the density, specific heat, thermal conductivity, and absorption coefficient of the material respectively. For simplification, the irradiated material is defined as uniformly absorbing. Thus, the power density in equation 1 can be described by the Beer-Lambert law. Taking the surface reflectivity of the irradiated material into account by an additional term, the power density *I(x,t)* can be expressed as

$$I(x,t) = I_0(t) exp(-\alpha \cdot x)(1-R), \quad (2)$$

where I_0 is the output power density of the laser and *R* is the reflectivity. The surface boundary conditions at points 1 and 4 are given by

$$\vec{n}\left(\kappa \frac{\partial T}{\partial t}\right) = h(T_{ext} - T), \quad (3)$$

with *n* as the normal vector, *h* as the convective heat transfer coefficient, and T_{ext} as the ambient temperature.

As demonstrated by Darif and Semmar [9], using a good approximation of the shape of the laser pulse in the time-domain is crucial to get realistic results. Here, we model the output power density of the pulsed excimer laser by the equation

$$I_0(t) = \exp\left(-\exp\left(-\frac{(t-t_c)}{w}\right) - \left(\frac{t-t_c}{w}\right) + 1\right), \quad (4)$$

where t_c is the time of the pulse peak and *w* is the pulse width. The best fit between the

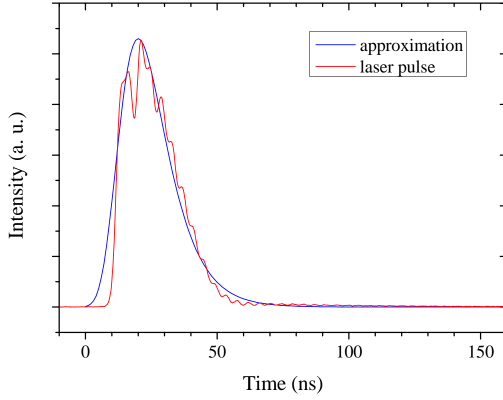

Figure 3. Comparison of the approximated shape of the laser pulse and the measured signal.

measured laser pulse and equation 4 is reached with values of $t_c = 20$ ns and $w = 8.96$ ns. Figure 3 depicts the comparison of the measured laser pulse and the approximation.

For further improvement of the model, the phase transition of the irradiated a-Si layer is implemented into the model. Therefore, all variables which are affected by the phase transition are divided into two terms in a way as

$$A \cdot (1 - H(T)) + B \cdot H(T)\ . \qquad (5)$$

In this term A and B represent the values for the solid state and the liquid state of the affected variable respectively. $H(T)$ is a Heaviside step function which is shifted to the melting point of a-Si. In addition, we model the latent heat L of the phase transition by adding the term

$$L_{a-Si} \frac{\partial H}{\partial T} \qquad (6)$$

to the specific heat $C_{p,a\text{-}Si}$ of a-Si.

4. Use of COMSOL Multiphysics

The described model is realised in COMSOL Multiphysics version 4.2 using a time-dependent study in the application mode Heat Transfer in Solids (ht). The sample geometry is made as previously shown in Figure 2. The material parameters for the silicon dioxide layer and the silicon wafer are taken from the COMSOL material library. Unfortunately, a-Si is not included in this library, and thus, the necessary parameters are taken from the literature [10-13]. An overview of these parameters with description and corresponding reference is given in Table 1.

To implement the laser caused heating, a heat source Q is added to the application mode ht. The heat source is given by the combination of equation 2 and 4. Because the absorption length of ultraviolet light in a-Si is extremely short, the heat source Q is only valid for the

Tabel 1. Overview of the user-implemented parameters of amorphous silicon.

Name	Expression	Description
$\kappa_{a\text{-}Si}$	$(1.3 \cdot 10^{-11}$ (T – 900 K)^3 + $1.3 \cdot 10^{-9}$ (T – 900 K)^2 + $1.0 \cdot 10^{-6}$ (T – 900 K) + $1.0 \cdot 10^{-2}$) W cm^{-1} K^{-1}	Thermal conductivity of a-Si [10]
$C_{p,a\text{-}Si}$	(0.171 T/1865 K + 0.952) J g^{-1} K^{-1}	Specific heat of a-Si [11]
$T_{m,a\text{-}Si}$	1440 K	Melting point of a-Si [11]
$\rho_{a\text{-}Si}$	2260 kg m^{-3}	Density of a-Si [12]
$L_{a\text{-}Si}$	1320 J g^{-1}	Latent heat of a-Si [12]
$R_{a\text{-}Si,l}$	0.58	Reflectivity of solid a-Si [12]
$R_{a\text{-}Si,s}$	0.72	Reflectivity of liquid a-Si [12]
$\alpha_{a\text{-}Si}$	$1.75 \cdot 10^{-6}$ cm^{-1}	Absorption coefficient of a-Si [13]

interval i1 to reduce the calculation costs.

As mentioned before, at point 1 convective cooling occurs. It is modelled by the predefined external natural convection settings in COMSOL. In these settings, a horizontal plate with a diameter of $d = 20$ cm is chosen, because this matches the wafer we used in our previous experiments best. The initial temperature of the three intervals i1-i3 is defined in the global parameter T_{Probe}. This parameter is changed in steps of 25 K from 300 K to 500 K by a parametric sweep to allow analysis of the influence of the initial sample temperature on the results of the ELA.

The point 1 must be coupled to the model in a specific way to model the change of the reflectivity at the surface of the sample caused by the phase transition. This is done by the COMSOL model coupling integration operator (intop). Each point in the model can then access information on the surface reflectivity via this operator.

Due to the high absorption coefficient of a-Si, the mesh of interval i1 is chosen with an extremely fine mesh element size of 0.1 nm to satisfy the high spatial change of the absorbed laser power. However, the mesh element size in the silicon dioxide and the silicon wafer underneath can be set to be much coarser.

The short pulse duration of the excimer laser implies fast changes of the power density in the time domain. In addition, the phase transition also causes fast changes of several variables. Therefore, a very fine time stepping during the laser pulse and the possible melt period afterwards is necessary to enable a reasonably low convergence of the solver. We define an initial time step of 100 fs and a max-

imum step size of 10 ps to satisfy the required fine time stepping in our model. Subsequently, the time stepping can be increased as no further fast changes in the time or spatial domains occur. Thus, we define the time stepping by an exponential growth function for the time after the melt period.

5. Results and Discussion

As described above, we want to extract information on melt duration, melt threshold, melt depth, onset time to melt, and the spatial distribution of the temperature from our simulations. These values and their comparison to the corresponding experimental values are presented in the following subsections.

5.1 Melt Duration and Melt Threshold

The melt duration is plotted in Figure 4a as a function of the energy density of the laser with the initial sample temperature as parameter. There are only the graphs of three of the nine temperatures used for the simulations plotted in this figure to enhance its clarification. Apparently, the results show a clear melt threshold value E_{th} for the energy density. The value for this threshold is $E_{th} = 88.5$ mJ/cm^2 at

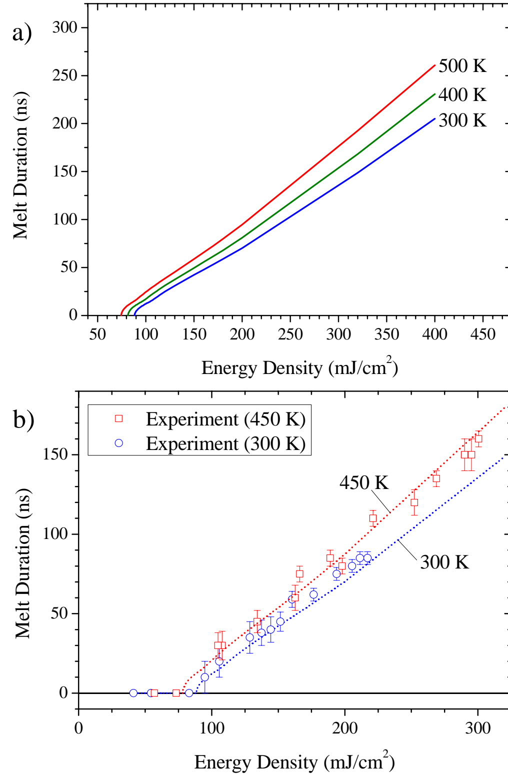

Figure 4. Melt duration as a function of the energy density. Results of the simulations for different initial sample temperatures (a) and comparison between simulation (dotted lines) and experiment at temperatures of 300 K and 450 K (b).

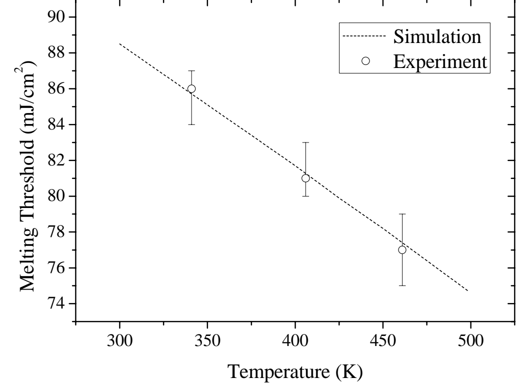

Figure 5. Comparison of the results from the simulations and the experiments for the temperature-dependent shift of the melt threshold value of the energy density.

room temperature. For energy densities below E_{th} the sample stays completely solid because the heat which is introduced by the laser is insufficient to melt the sample. However, an almost linear increase of the melt duration with a slope of approximately $\partial t/\partial E = 625$ ns cm^2 J^{-1} with increasing energy density is observed for energy densities above E_{th}. Both the value of E_{th} and the behaviour of the melt duration are in excellent agreement with the results of our ELA experiments. As shown in Figure 4b, the values for the melt duration which are measured by TRRM differ only by a few nanoseconds from the results of our simulations. These differences are within the limits of the uncertainty of the TRRM analysis.

In addition, the graph of the melt duration shows a clear decrease of E_{th} with rising initial sample temperature. This relationship is plotted in Figure 5. With rising initial temperature the sample has more thermal energy at the beginning of the ELA. Consequently, less energy from the laser is necessary to reach the melt threshold. Again, this behaviour agrees well with our experimental results as can be seen in Figure 5.

5.2 Onset Time to Melt

The onset time to melt as a function of the energy density is shown in Figure 6a at different initial sample temperatures. Again, there are only the graphs of three of the nine temperatures used for the simulations plotted in this figure to enhance its clarification. As shown in this figure, the onset time to melt has a starting value of almost $t_{on} = 28$ ns for an energy density which is close to E_{th}. Figure 6a also illustrates that the onset time to melt depends on the energy density. The sample is heated faster with increasing energy density leading to a reduced onset time to melt. However, the onset

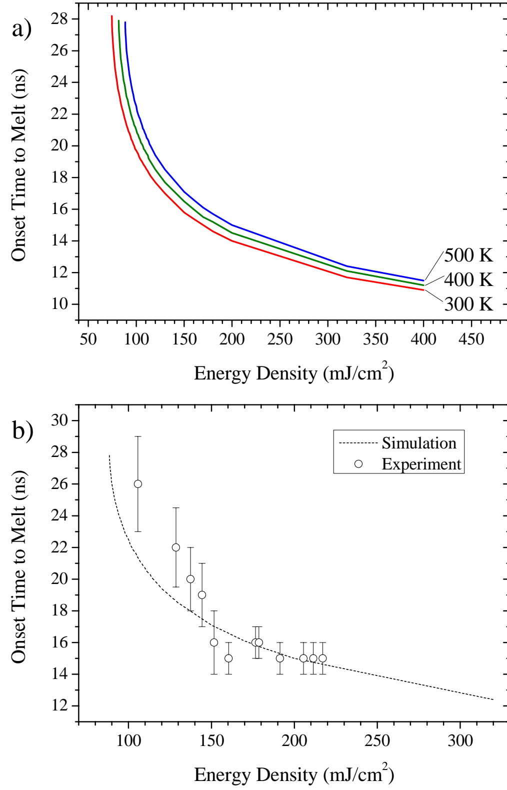

Figure 6. Onset time to melt as a function of the energy density of the laser. Results from the simulations for different initial sample temperatures (a) and comparison between simulation and experiment at room temperature (b).

time seems to level at a value around several nanoseconds with increasing energy density.

As depicted in Figure 6b, the results from our simulations coincide with the results from our experiments. Especially for energy densities above $E = 170$ mJ/cm^2 hardly any discrepancy is noticeable. For smaller energy densities the values differ by a few nanoseconds. This is most probably due to the huge uncertainty caused by the low signal to noise ratio of the TRRM setup.

5.3 Melt Depth

The melt depth is defined as the maximum depth (x value) at which the aforementioned Heaviside step function equals H = 0.5. The results of this interpretation are plotted in Figure 7 as a function of the energy density at an initial sample temperature of $T_{\text{init}} = 300$ K. Again, the graph shows a clear melt threshold and an almost linear growth with a slope of $\partial d_m/\partial E = 43$ µm cm^2 J^{-1} with increasing energy density.

Figure 7 also includes the values for the melt depth which are extracted from SEM images of some samples we used for our ELA experiments. Because there is only a hardly

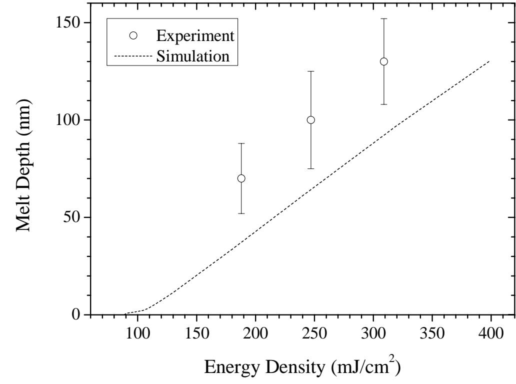

Figure 7. Comparison between results from the simulations and experiments concerning the melt depth.

noticeable contrast between microcrystalline silicon and a-Si in the SEM images, the extracted values ehibit an enormous uncertainty. Unfortunately, there is a huge difference in the melt depth between the calculated values and the extracted ones which can not only be explained by the uncertainty. Remarkably, the three measured values have an equal difference of approximately $\Delta d_m = 30$ nm. Thus, most probably a systematic error causes this offset. We believe that this offset is due to explosive crystallisation which is often observed during ELA of a-Si [14].

As described by Polman et al. [15], explosive crystallisation is a self-propagating melting and re-solidification process driven by the difference in the latent heat of amorphous and crystalline silicon. Since we do not modell this change of the latent heat, explosive crystallisation is not included in our simulations. Therefore, the results from our ELA experiments exhibit a larger melt depth than the results from our simulations.

5.4 Thermal Load of the Substrate

The thermal load of the substrate is also extracted from the results of our simulations. It is presented in Figure 8. In this figure, the thermal load is given as a surface plot because it is a function of both the energy density of the laser and the distance to the surface. It is obvious from Figure 8 that the temperature of the sample rapidly drops with increasing distance to the surface. This decline has two different slopes due to the different material parameters for the a-Si layer (0 nm – 250 nm) and the SiO_2 layer (250 nm – 1250 nm). These results agree well with observations made by Sameshima et al. [16]. Furthermore, Figure 8 shows a clear decrease of the dependence on the energy density of the laser with increasing distance to the surface. For example, irradiat-

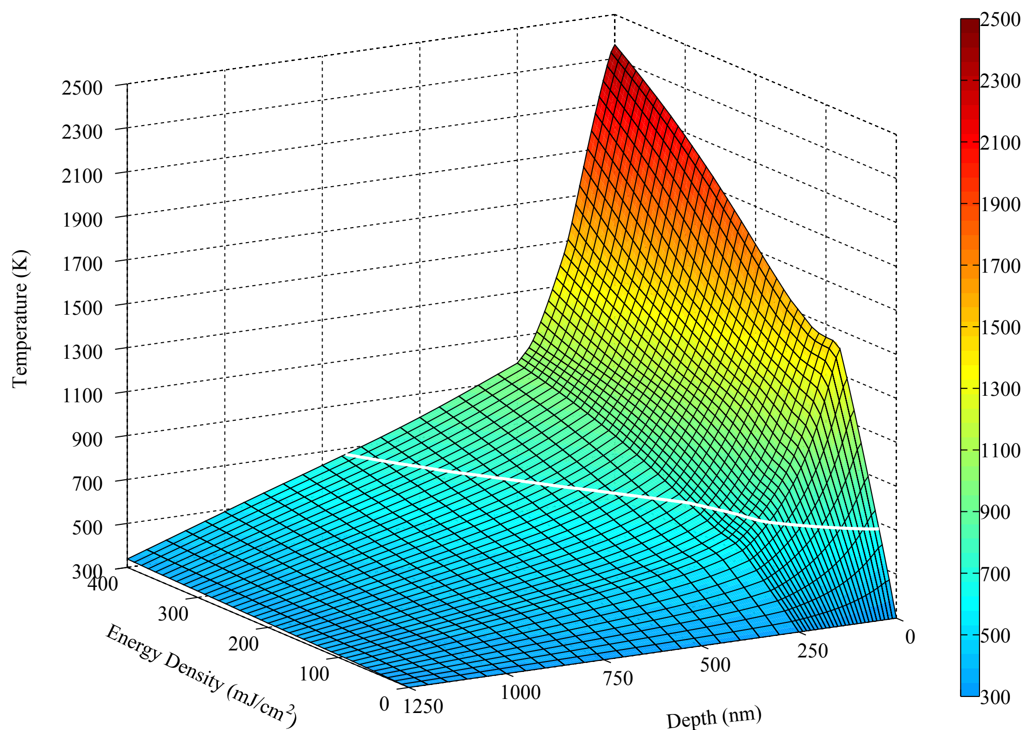

Figure 8 Spatial distribution of the maximum sample temperature vs. the distance to the surface of the sample and the energy density of the laser. The white curve represents the isoline for 673 K.

ing the sample with an energy density of $E = 400$ mJ/cm^2 is leading to the result that the bottom of the SiO_2 layer is heated only by approximately $\Delta T_{bot} = 40$°C, whereas the top of the SiO_2 layer exhibits a temperature rise by almost $\Delta T_{top} = 700$°C.

As a main benefit, Figure 8 can be used to decide on several ELA process parameters. For instance, Figure 8 helps finding maximum values for the energy density of the laser during ELA of samples without a thermal buffer layer (e. g. SiO_2) between the a-Si layer and the heat-sensitive substrate. In addition, it also gives information on the minimum thickness of the SiO_2 layer for samples which contain such a thermal buffer layer on top of the heat-sensitive material. This relationship of energy density and distance to the surface concerning the sample temperature is illustrated by the white line in Figure 8 valid for the aforementioned maximum thermal load of $T_{max} = 400$°C (673 K). As can be seen, the thermal load for the material beneath the SiO_2 layer (x = 1250 nm) is negligible for our sample configuration.

6. Conclusions

We successfully modelled ELA of a-Si layers. The results of our simulations were compared to the results of our previous ELA experiments and it was shown that the model is in excellent agreement with our experiments for the melt threshold, the melt duration, and the onset time to melt. Therefore, our model provides valid results. Though a static offset between the results from the simulations and the results from the experiments concerning the melt depth was detected, it did not reduce the plausibility of our model because it could be explained by explosive crystallisation phenomenon. Thus, valuable predictions of the thermal load in our samples can be gained with the help of our model.

7. References

[1] J. B. Boyce and P. Mei, Laser Crystallization for Polycrystalline Silicon Device Applications, in *Technology and Applications of Amorphous Silicon*, edited by R. A. Street, New York: Springer, pp. 94-144 (1999)

[2] W. W. Duley, *UV Lasers: effects and applications in materials science*, Cambridge: University Press, pp. 345-349 (1996)

[3] G. Yaron and L. D. Hess, Application of laser annealing techniques to increase channel mobility in silicon on sapphire transistors, *Appl. Phys. Lett.*, **36**(3), pp. 220-222 (1980)

[4] R. Pätzel et al., Activation of Silicon Wafer by Excimer Laser, *Advanced Thermal Processing of Semiconductors (RTP), 2010 18th International Conference on*, pp.98-102 (2010)

[5] A. Florakis et al., Formation of silicon ultra shallow junction by non-melt excimer laser treatment, *Solid-State Electronics*, **54**(9), pp. 903-908 (2010)

[6] J. Förster et al., Investigation of the thermal coefficient of electrical resistance and 1/f noise of laser-annealed a-Si layers, *Advanced Thermal Processing of Semiconductors (RTP), 2010 18th International Conference on*, pp.104-109 (2010)

[7] G. E. Jellison et al., Time-resolved reflectivity measurements on silicon and germanium using a pulsed excimer KrF laser heating beam, *Phys. Rev. B*, **34**(4), pp. 2407-2415 (1986)

[8] P. Baeri and S. U. Camisano, Heat Flow Calculations, in *Laser Annealing of Semiconductors*, New York: Academic Press, pp. 75-109 (1982)

[9] M. Darif and N. Semmar, Numerical Simulation of Si Nanosecond Laser Annealing by COMSOL Multiphysics, *Proceedings of the COMSOL Conference 2008 Hannover* (2008)

[10] H. C. Webber et al., Computer simulation of high speed melting of amorphous silicon, *Appl. Phys. Lett.*, **43**(7), pp. 669-671(1983)

[11] C. K. Ong et al., Calculations of Melting Threshold Energies of Crystalline and Amorphous Materials Due to Pulsed-laser Irradiation, *Mater. Sci. Eng.*, **79**(11), pp. 79-85 (1986)

[12] C. J. Shih et al., Phase field modeling of excimer laser crystallization of thin silicon films on amorphous substrates, *J. Appl. Phys.*, **100**(5), pp. 053504 (2006)

[13] G. E. Jellison et al., Optical absorption of silicon between 1.6 and 4.7 eV at elevated temperatures, *Appl. Phys. Lett.* **41**(2), pp. 180-182 (1982)

[14] Chil-Chyuan Kuo, Observation of explosive crystallization during excimer laser annealing using in situ time-resolved optical reflection and transmission measurements, *J. Mater. Process. Technol.*, **209**(6), pp. 2978-2985 (2009)

[15] A. Polman et al., Epitaxial explosive crystallization of amorphous silicon, *Appl. Phys. Lett.*, **55**(11), pp. 1097-1099 (1989)

[16] T. Sameshima et al., Measuring the Temperature of a Quartz Substrate during and after Pulsed Laser-Induced Crystallization of a-Si:H, *Jpn. J. Appl. Phys.*, **28**(12), pp. 2131-2133 (1989)